Energy Advances

ROYAL SOCIETY OF CHEMISTRY

PAPER

View Article Online
View Journal | View Issue

Cite this: *Energy Adv.*, 2025, 4, 1383

Next-generation dual absorber solar cell design with Ca_3AsI_3 and Sr_3PBr_3 perovskites and MoO_3 HTL achieves superior efficiency above 29%

Sahjahan Islam,[a] Jannati Islam Chy,[a] Dipika Das Ria,[a] Abu Bakkar,[b] Md. Faruk Hossain,[c] Ahmad Irfan,[d] Aijaz Rasool Chaudhry[e] and Md. Ferdous Rahman *[b]

This research explores the photovoltaic performance of four different perovskite solar cell (PSC) architectures, with emphasis on how material selection, absorber layer thickness, defect and acceptor densities, interface imperfections, and temperature fluctuations influence device efficiency. Energy band alignment analyses were conducted to enhance charge separation and extraction. Among the configurations, the device incorporating dual absorbers Sr_3PBr_3 and Ca_3AsI_3 exhibited the highest efficiency. Analysis of absorber thickness effects indicated maximum power conversion efficiencies (PCEs) of 20.71% for device-i (FTO/CdS/Sr_3PBr_3/Au) and 19.75% for device-ii (FTO/CdS/Ca_3AsI_3/Au) at a thickness of 1.0 μm. In contrast, device-iv (FTO/CdS/Ca_3AsI_3/Sr_3PBr_3/MoO_3/Au), which employed both a dual-absorber design and a MoO_3 hole transport layer (HTL), achieved an optimal PCE of 29.77% with each absorber layer also at 1.0 μm thickness. The investigation into defect densities revealed that increased defect levels significantly diminished performance. Device-iv stood out for its enhanced stability and efficiency, resulting from fine-tuned acceptor density and effective interface defect mitigation. Temperature analysis showed a general decline in efficiency with increasing temperature, though device-iv maintained relatively higher thermal stability. Overall, the study highlights the critical role of dual absorber layers, optimized geometries, effective HTLs, and minimized defect concentrations in advancing the efficiency and durability of high-performance PSCs.

Received 19th May 2025,
Accepted 9th September 2025

DOI: 10.1039/d5ya00137d

rsc.li/energy-advances

1. Introduction

The quest for efficient and cost-effective solar energy technologies has advanced remarkably in recent years, driven by the global transition to renewable energy and efforts to reduce reliance on fossil fuels while tackling urgent environmental challenges.[1,2] Among photovoltaic technologies, perovskite solar cells (PSCs) stand out as transformative innovations, offering high performance, low PSC manufacturing cost, and scalability due to their superior optical, structural, and electrical properties.[3–7] The power conversion efficiency (PCE) of PSCs has significantly grown recently, rising from 3.8% in 2009 to over 25% in recent studies, indicating their promise for high-efficiency solar energy conversion.[8–10] Lead-based perovskites have achieved remarkable efficiency benchmarks; however, their practical application and broader adoption are hindered by the toxicity of lead and the inherent instability of these materials.[11–14] In contrast, inorganic perovskites, renowned for their exceptional optical and electrical properties, mechanical stability, and non-toxic nature, are regarded as a promising absorber material for photovoltaic cells, with the potential to address these challenges.[15,16] The main unresolved issues with organic perovskite cations are their volatility and significant thermal instability, which limit their widespread commercial application. However, PSCs with organic–inorganic hybrids have significantly improved optical absorption, longer charge-carrier lifetimes, higher charge-carrier mobility, lower trap density, and lower exciton binding energy.[17,18] Inorganic perovskites with the formula A_3BX_3 exhibit a distinctive crystal

[a] Department of Physics & Astronomy Texas A & M University-Commerce 2200 Campbell St, Commerce, TX 75429, USA
[b] Advanced Energy Materials and Solar Cell Research Laboratory, Department of Electrical and Electronic Engineering, Begum Rokeya University, Rangpur 5400, Bangladesh. E-mail: ferdousapee@gmail.com
[c] Department of Physics, Rajshahi University of Engineering & Technology, Rajshahi 6204, Bangladesh
[d] Department of Chemistry, College of Science, King Khalid University, P.O. Box 9004, Abha 61413, Saudi Arabia
[e] Department of Physics, College of Science, University of Bisha, P.O. Box 551, 61922 Bisha, Saudi Arabia

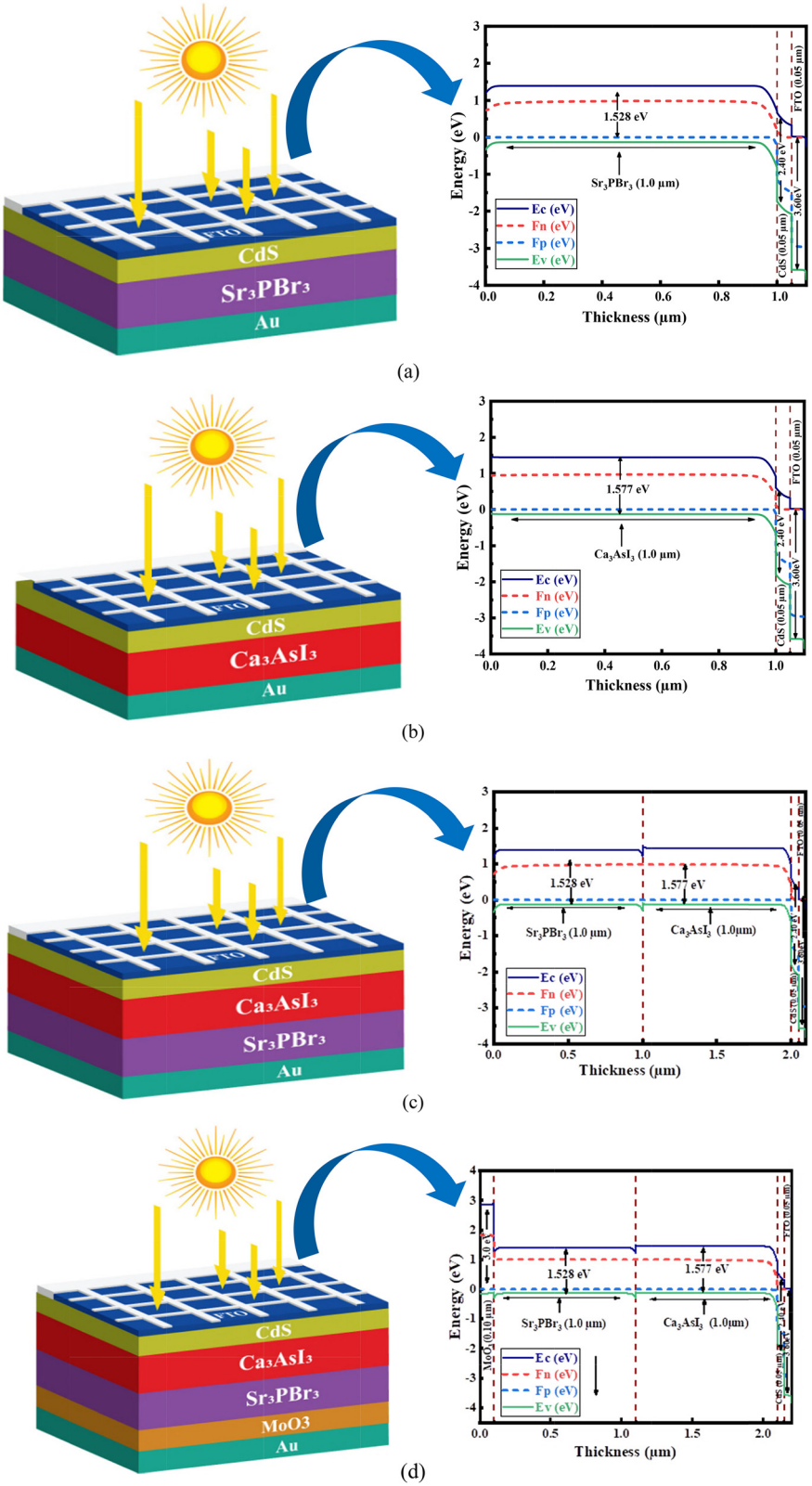

Fig. 1 The energy band diagram of (a) device-i, (b) device-ii, (c) device-iii, and (d) device-iv.

structure, where A signifies a larger inorganic cation, B denotes a smaller metal cation, and X represents an anion. The cation or halide atom at the A, B, or X site can be changed to enable pertinent customization and optimization of inorganic perovskites.[19,20] A compound with the chemical formula Ca_3AsI_3 is a member of the A_3BX_3 family has showed

Table 1 Input parameters of the FTO, ETLs, BSF and absorber layers

Parameters	FTO[28,52]	CdS[53]	Ca_3AsI_3[20]	Sr_3PBr_3[20]	MoO_3[54]
Thickness (nm)	50	50	1000	1000	0.1
Band gap, E_g (eV)	3.6	2.4	1.577	1.52	3.0
Electron affinity, χ (eV)	4.5	4.2	3.89	4.16	2.50
Dielectric permittivity (relative), ε_r	10	10	5.65	5.28	12.50
CB effective density of states, N_C (cm^{-3})	2×10^{18}	2.2×10^{18}	8.33×10^{19}	1.185×10^{19}	2.2×10^{18}
VB effective density of states, N_V (cm^{-3})	1.8×10^{19}	1.8×10^{19}	1.6×10^{19}	1.66×10^{19}	1.8×10^{19}
Electron mobility, μ_n ($cm^2\ V^{-1}\ s^{-1}$)	100	100	50	25	25
Hole mobility, μ_h ($cm^2\ V^{-1}\ s^{-1}$)	20	25	25	20	100
Shallow uniform acceptor density, N_A (cm^{-3})	0	0	1×10^{17}	1×10^{18}	1×10^{17}
Shallow uniform donor density, N_D (cm^{-3})	1×10^{18}	1×10^{17}	0	0	0
Defect density, N_t (cm^{-3})	1×10^{14}	1×10^{14}	1×10^{12}	1×10^{12}	1×10^{14}

optoelectronic features including a direct band gap of 1.58 eV, revealing the semiconducting properties.[21,22] However, certain limitations restrict its widespread implementation. Ca_3AsI_3 exhibits challenges related to structural and thermal stability, particularly under ambient conditions, which may impede its scalability in practical applications. Additionally, its bandgap, while suitable, has been noted to be less tunable compared to other perovskites, which limits its adaptability for specific solar cell architectures such as tandem designs.[16,23] To address the challenges associated with Ca_3AsI_3, researchers have explored alternative nontoxic perovskite absorber materials, such as strontium phosphide bromide (Sr_3PBr_3).[24] This compound, featuring a bandgap of 1.528 eV, has been recognized for its remarkable light-absorbing capabilities across the visible spectrum of the electromagnetic range. The lower bandgap of Sr_3PBr_3, compared to $CsPbI_3$, enhances its ability to capture a greater number of photons within the visible spectrum, making it a more effective absorber material for photovoltaic applications. Its compatibility with the visible spectral range positions Sr_3PBr_3 as a promising candidate for improving solar cell efficiency.[3,20,25]

Ca_3AsI_3 and Sr_3PBr_3 were selected as absorber materials in this study due to their complementary bandgaps, which together enhance the overall light-harvesting capability of the device. Both materials exhibit favorable optoelectronic properties, including high absorption coefficients and efficient charge carrier transport, while being lead-free, making them environmentally benign alternatives to conventional perovskites. Although these materials have been relatively rarely studied, recent experimental and simulation investigations[26–28] indicate their stability and suitability as absorbers in high-performance PSCs. This combination of properties motivated their selection for the proposed dual-absorber architecture.

From a stability standpoint, both Ca_3AsI_3 and Sr_3PBr_3 benefit from their fully inorganic composition, which imparts improved thermal and environmental tolerance compared to hybrid organic–inorganic perovskites. Nonetheless, potential degradation mechanisms such as moisture- and oxygen-induced surface reactions, halide migration under bias, and defect formation at grain boundaries may still occur under prolonged operation. These effects can be mitigated through encapsulation, interface passivation, and controlled processing to minimize defect densities. Given their thermal stability and

Table 2 Data for interface parameters used in the Sr_3PBr_3 and Ca_3AsI_3 double absorber based solar cell[28,52,55]

	Interfaces			
Parameter	Sr_3PBrI_3/CdS	Ca_3AsI_3/CdS	Sr_3PBr_3/Ca_3AsI_3	MoO_3/Sr_3PBrI_3
Defect type	Neutral	Neutral	Neutral	Neutral
σ_e (cm^2)	1×10^{19}	1×10^{19}	1×10^{19}	1×10^{19}
σ_h (cm^2)	1×10^{19}	1×10^{19}	1×10^{19}	1×10^{19}
E_r	0.6	0.6	0.6	0.6
Total defect density	10^{10}	10^{10}	10^{10}	10^{10}
Energetic distribution	Single	Single	Single	Single
Working temperature (K)	300	300	300	300

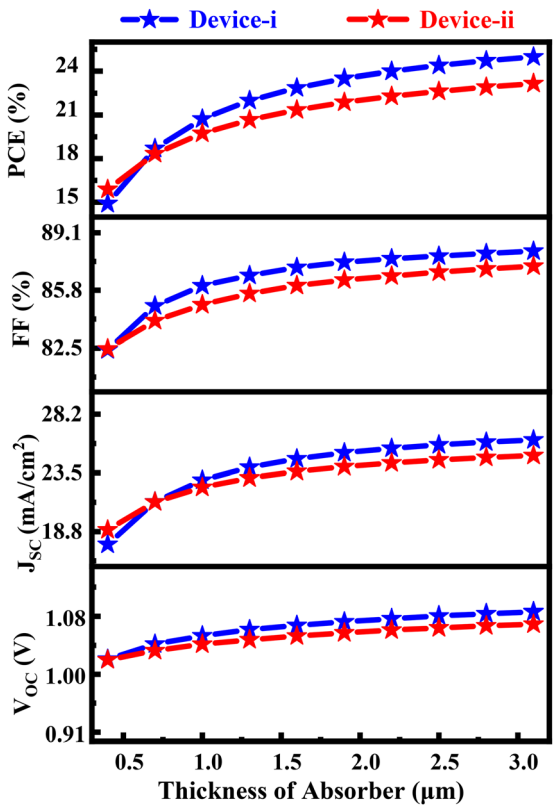

Fig. 2 Impact of the thickness variation of Sr_3PBr_3 (device-i) and Ca_3AsI_3 (device-ii) on photovoltaic parameters.

compatibility with low-temperature deposition, the proposed absorbers are well-suited for integration into scalable device architectures, provided that appropriate protective and passivation strategies are employed.

The utilization of bilayer or multilayer heterojunction structures can help to overcome the efficiency restrictions of single-junction solar cells, which are limited by the Shockley–Queisser limits and the second law of thermodynamics.[29] A remarkable power conversion efficiency (PCE) of 31.91% was demonstrated by Tinedert *et al.* using a double-layer device that included $CsPbI_3$ and $RbGeI_3$.[30] A multi-junction PSC made of $C_{60}/CsPbI_x$-$Br_{3-x}/FAPbI_yBr_{3-x}$ was also created by Zhang *et al.*, who achieved a noteworthy PCE of 17.48%.[31] Hajjiah *et al.* also performed device calculations and found that a dual-layer structure of $CsPbI_3/FAPbI_3$ may achieve an efficiency of 20%.[32] Moreover, Khatoon *et al.* used SCAPS-1D simulations to study bilayer PSCs, such as $CsPbIBr_2/CsPbI_2Br$ and $CsPbI_3/MAPbI_3$, and discovered that these designs provided PCEs above 33%, far outperforming single-junction PSCs.[33,34]

This study highlights the novel double-absorber solar cell configuration that synergistically combines two perovskite materials, namely, Ca_3AsI_3 and Sr_3PBr_3 while addressing the limitations that hinder device performance. Advanced optimization techniques and numerical modeling are employed to enhance solar efficiency, targeting performance improvements that are often unachievable even in many optimal perovskite tandem device configurations. Despite their potential, high-performing tandem devices typically require multiple material layers with precise band alignment, a complexity that can lead to energy losses and reduced performance. A more sensible and efficient approach is to employ a dual absorber layer with well-matched band alignment to adjacent layers, removing the difficulties with fabrication costs and processing techniques.[35] Moreover, the inclusion of molybdenum trioxide (MoO_3) as the hole transport layer (HTL) further enhances the cell's overall performance by improving charge extraction and reducing interfacial losses owing to its excellent optical properties and suitable work function.[36–39] The proposed solar cell

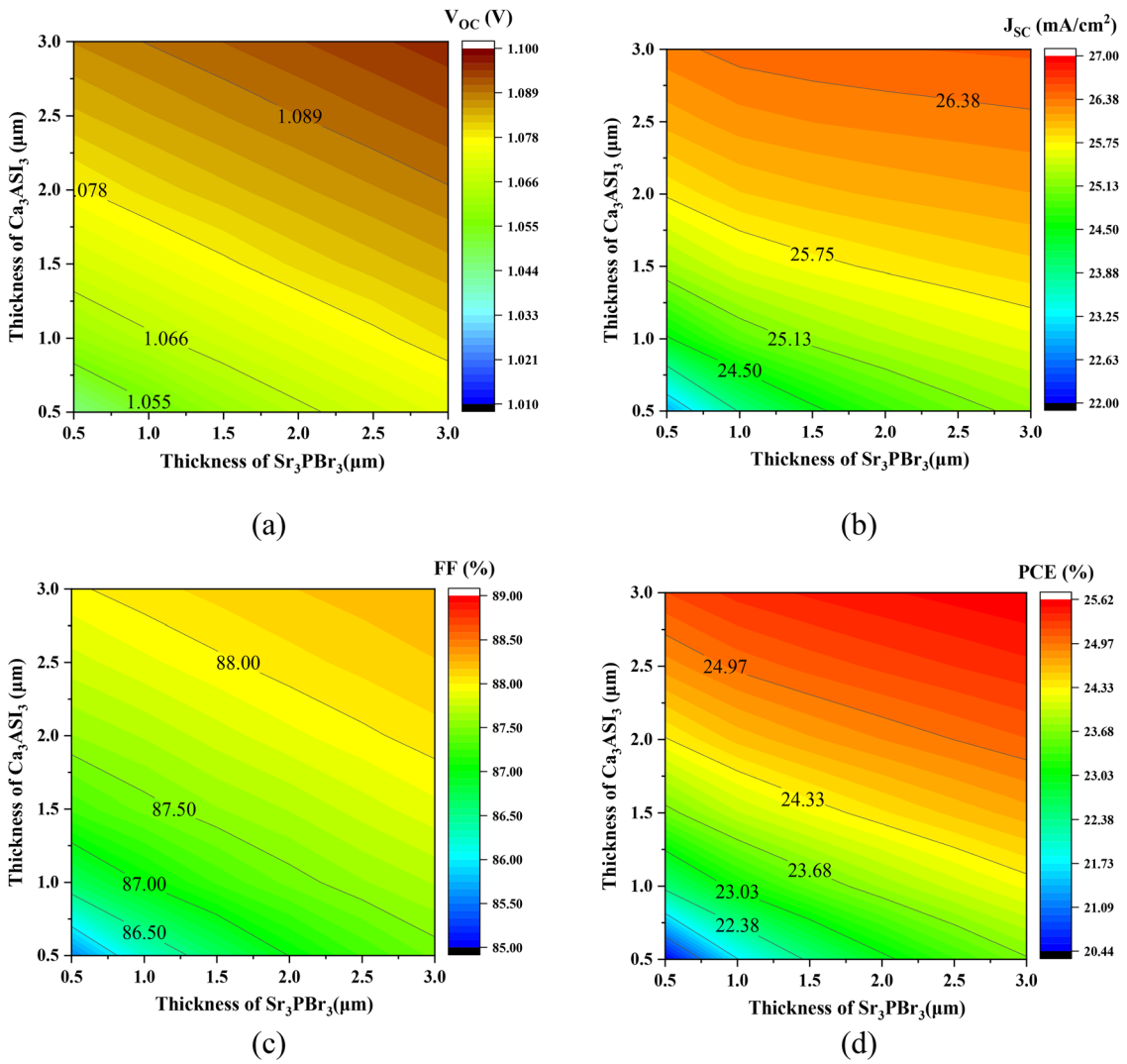

Fig. 3 Role of thickness variation of Sr_3PBr_3 and Ca_3AsI_3 (device-iii) on the photovoltaic parameters, (a) V_{OC}, (b) J_{SC}, (c) FF, and (d) PCE.

structures were systematically designed and analyzed using the SCAPS-1D simulation software, providing insights into their potential efficiencies and operational mechanisms.

In this study, we propose a novel lead-free dual-absorber perovskite solar cell employing Ca_3AsI_3 and Sr_3PBr_3 as complementary absorbers combined with a MoO_3 hole transport layer (HTL). Unlike conventional tandem or bilayer devices based on $CsPbI_3$/$FAPbI_3$ or other lead-containing systems, the present architecture exploits the distinct bandgaps of Ca_3AsI_3 and Sr_3PBr_3 to broaden the absorption spectrum, enhance charge carrier extraction, and reduce recombination losses. This dual-absorber configuration demonstrates a viable pathway toward environmentally sustainable, high-efficiency perovskite photovoltaics, representing a significant advancement in the design of lead-free, multi-absorber solar cells.

The study encompasses four distinct solar cell configurations: (i) FTO/CdS/Sr_3PBr_3/Au, (ii) FTO/CdS/Ca_3AsI_3/Au, (iii) FTO/CdS/Ca_3AsI_3/Sr_3PBr_3/Au, and (iv) FTO/CdS/Ca_3AsI_3/Sr_3PBr_3/MoO_3/Au. Initially, single-absorber PSCs are simulated using two different absorbers. Subsequently, these absorbers are incorporated into dual-absorber solar cells, and finally, a HTL is added to enhance performance. By leveraging the SCAPS-1D platform, we conducted a comprehensive performance analysis of these architectures to identify the optimal design parameters and material configurations. The results indicate that the innovative design with the inclusion of both Ca_3AsI_3 and Sr_3PBr_3 in a double-absorber configuration which is combined with MoO_3 as the HTL, achieves an unprecedented efficiency exceeding 29% highlighting the potential of the dual absorber layer design with improved performance over conventional single-junction configurations.

2. Materials and methodology

SCAPS-1D is a powerful tool for modeling and designing PSCs, enabling comprehensive data analysis and optimization of their optoelectronic properties.[40] In this study, the device structure is meticulously modeled, and its key properties are

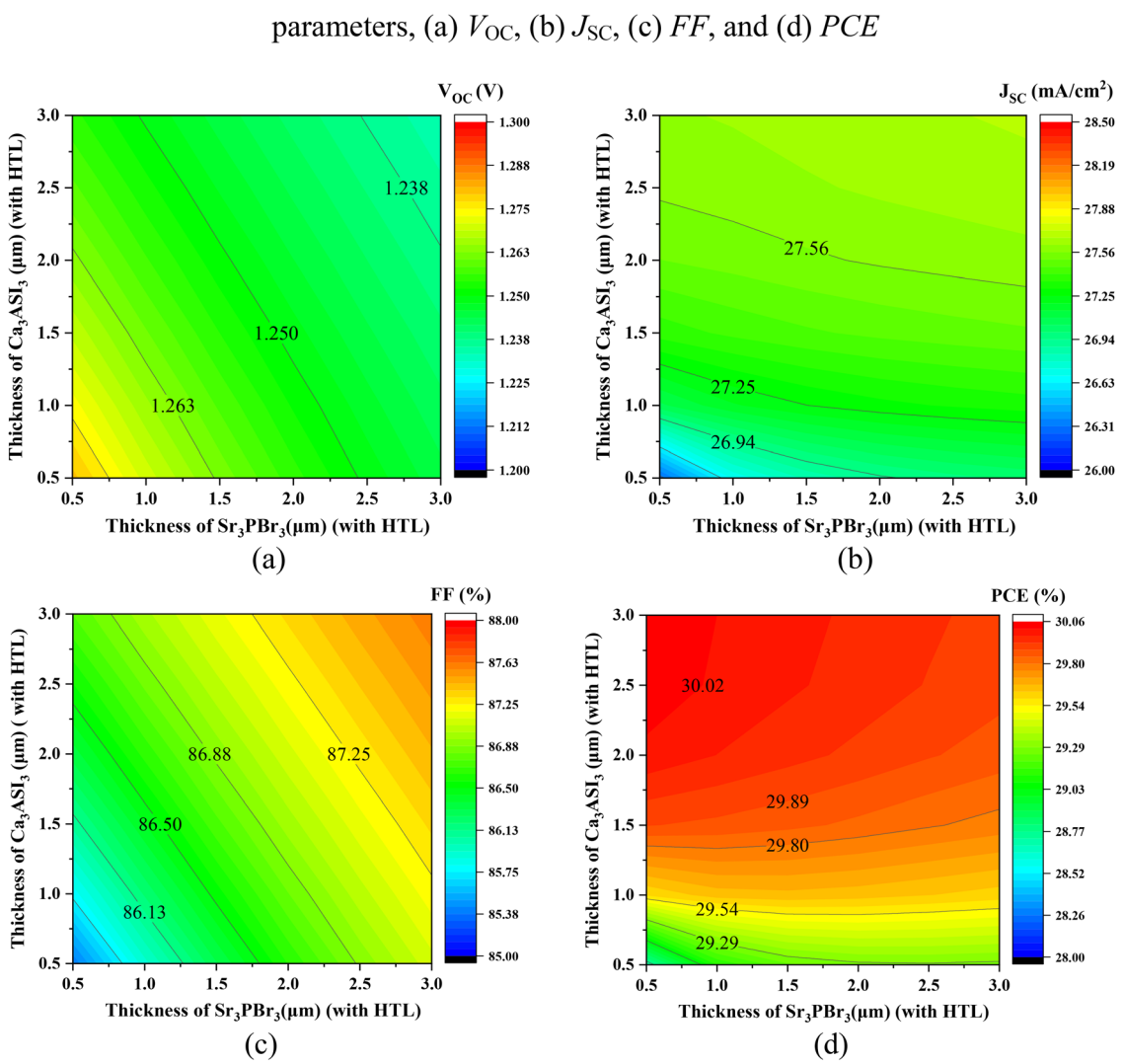

Fig. 4 Influence of thickness variation of Sr_3PBr_3 and Ca_3AsI_3 (device-iv) on the photovoltaic parameters, (a) V_{OC}, (b) J_{SC}, (c) FF, and (d) PCE.

thoroughly assessed using SCAPS-1D software,[41] allowing for a comprehensive evaluation of its optoelectronic performance. This approach facilitates an in-depth understanding of the device's behavior and aids in optimizing its efficiency for practical applications. In order to accurately calculate the current density–voltage (*J–V*) characteristics, quantum efficiency (QE), energy bands, and other relevant parameters, the simulation solves key semiconductor equations, including Poisson's equation (eqn (1)) and the continuity equations (eqn (2) and (3)).[7,42–44] These equations are essential for modeling the behavior of charge carriers within the device and for obtaining precise performance metrics.

$$\frac{d^2\phi(x)}{dx^2} = \left(\frac{q}{\varepsilon_0\varepsilon_r}\right)\left(p(x) - n(x) + N_D - N_A + \rho_p - \rho_n\right) \quad (1)$$

$$\frac{dJ_n}{dx} = G_n - R_n \quad (2)$$

$$\frac{dJ_P}{dx} = G_p - R_p \quad (3)$$

Where Ψ, q and ε are defined as an electrostatic potential, an electron charge, and dielectric permeability, respectively, N_A/N_D represent the concentrations of ionized donors/ionized acceptors, ρ_p (ρ_n) is presented as hole (electron) distribution, and $p(x)/n(x)$ illustrated hole/electron density distribution (in terms of thickness x). In addition, J_n/J_p stands for current densities of electron/hole, G_n/G_p defines optical carrier (electron/hole) generation rate, and R_n/R_p are defined as the recombination rates associated with electron/hole.

In all simulations, defect states were modeled as neutral, as literature reports for similar halide perovskites indicate that neutral centers dominate Shockley–Read–Hall recombination in the relevant energy ranges.[45–48] Preliminary simulations including representative charged defect states produced <2% variation in PCE, suggesting that their influence is negligible under the present device conditions.

To ensure that the simulated results are physically realistic, all key material and interface parameters were benchmarked against experimentally measured data and previously validated SCAPS-1D studies on comparable lead-free perovskite systems. This benchmarking covered optical constants, electronic transport parameters, and defect/interface characteristics, ensuring that the simulated device behavior reflects realistic photovoltaic operation. The agreement of our simulated parameter trends such as efficiency degradation with increased defect density and improved performance with optimized layer thickness—with reported experimental and theoretical observations[49–51] further supports the validity of the present modeling approach.

The purpose of this work is to investigate the fundamental insights of Ca_3AsI_3/Sr_3PBr_3 double layered PSC with MoO_3 serves as HTL. Initially, Ca_3AsI_3 and Sr_3PBr_3 were utilized as individual absorber layers in single-junction PSCs to optimize their performance. Following this, a dual-absorber layer configuration incorporating a Ca_3AsI_3/Sr_3PBr_3 heterojunction was investigated. In order to further improve device performance, MoO_3 was added as HTL to the double-layer PSC with the structure FTO/CdS/Ca_3AsI_3/Sr_3PBr_3/MoO_3/Au. This approach aims to improve the overall performance of the solar cell. The benefits of using multiple absorber layers with HTL in the solar cell architecture can be better understood by comparing the outcomes of various designs. Under the AM1.5G solar spectrum, the suggested structures are tested with a light power density of 1000 mW m^{-2}. Fig. 1(a)–(d) displays the schematic representations of the investigated four device configurations, such as (a) device-i: FTO/CdS/Sr_3PBr_3/Au; (b) device-ii: FTO/CdS/Ca_3AsI_3/Au; (c) device-iii: FTO/CdS/Ca_3AsI_3/Sr_3PBr_3/Au, and (d) device-iv: FTO/CdS/Ca_3AsI_3/Sr_3PBr_3/MoO_3/Au. Cadmium sulfide (CdS) is used as the electron transport layer (ETL) in all configurations because CdS enhances PSC efficiency by improving charge extraction, and reducing losses owing to its higher electron mobility.[44] Fluorine-doped tin oxide (FTO) is used as the transparent conducting oxide,[44] and gold (Au) is used as the metal back contact in all designs for confirming efficient capture and transfer of the produced charge carriers.[44] However, only Sr_3PBr_3 is used in device structure as absorber layer in Fig. 1(a) and (b) displays the structure of only Ca_3AsI_3 absorber layer. While, Fig. 1(c) and (d) both are depicted dual layers device structures but the latter device structure has optimized with MoO_3 HTL. The energy level diagrams of the materials used in the device architectures are shown in Fig. 1(a)–(d). Tables 1 and 2 provide

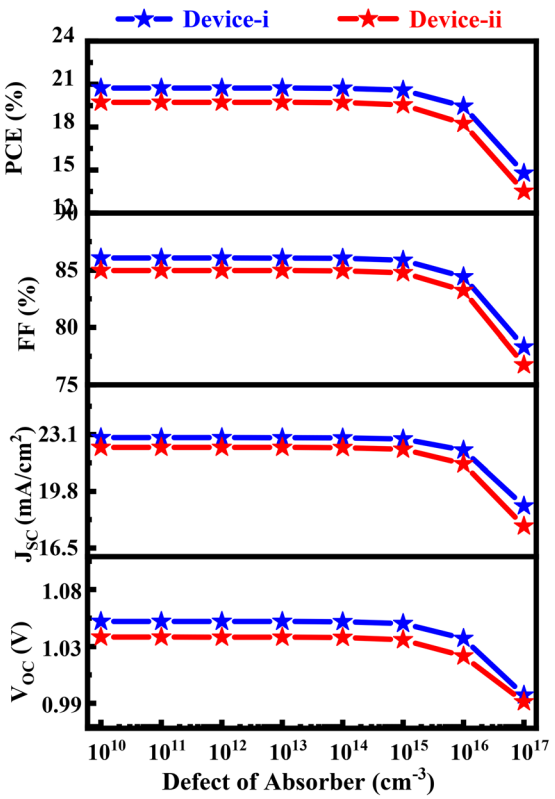

Fig. 5 Effect of defect variation of Sr_3PBr_3 (device-i) and Ca_3AsI_3 (device-ii) on photovoltaic parameters.

a detailed presentation of the device's and the materials' interface parameters, respectively.

3. Results and discussion

3.1. Bandgap alignment of the PSC devices

The Fig. 1 illustrates the cell and energy band diagrams for four different device structures, providing insights into the electronic properties of various photovoltaic materials. Fig. 1(a) shows the cell and band diagram for device i, where the conduction band minimum (CBM) of CdS is positioned at a higher energy level compared to the valence band maximum (VBM) of Sr_3PBr_3, indicating a potential for charge separation at the junction by promoting electron transfer from Sr_3PBr_3 to CdS at the interface. In Fig. 1(b), device ii displays a similar trend, with the VBM of Ca_3AsI_3 lower than the CBM of CdS, indicating a potential for charge separation, reduced with a larger bandgap of Ca_3AsI_3 that may lessen charge carrier mobility. Fig. 1(c), representing device iii, introduces both Ca_3AsI_3 and Sr_3PBr_3, creating multiple interfaces that improve light absorption and charge extraction, with energy alignment favoring charge separation.

Finally, Fig. 1(d) shows the cell and band diagram for device iv, where the inclusion of MoO_3 as a HTL[36–39] further enhances charge collection efficiency.[56] The variation in energy levels is primarily caused by the differences in the material bandgaps and interface characteristics, which influence the photovoltaic performance, including open-circuit voltage (V_{OC}) and short-circuit current density (J_{SC}). The bandgap values and energy alignments for the materials (Sr_3PBr_3, Ca_3AsI_3, and CdS) are crucial factors influencing the device efficiency and are tailored based on their optical absorption properties and electron transport characteristics.

3.2. Impact of absorber layer thickness on PV parameters

Fig. 2 illustrates how absorption layer thickness affects photovoltaic parameters for Ca_3AsI_3 (device-ii) and Sr_3PbBr_3 (device-i). In both devices, PCE rises with thickness, peaking

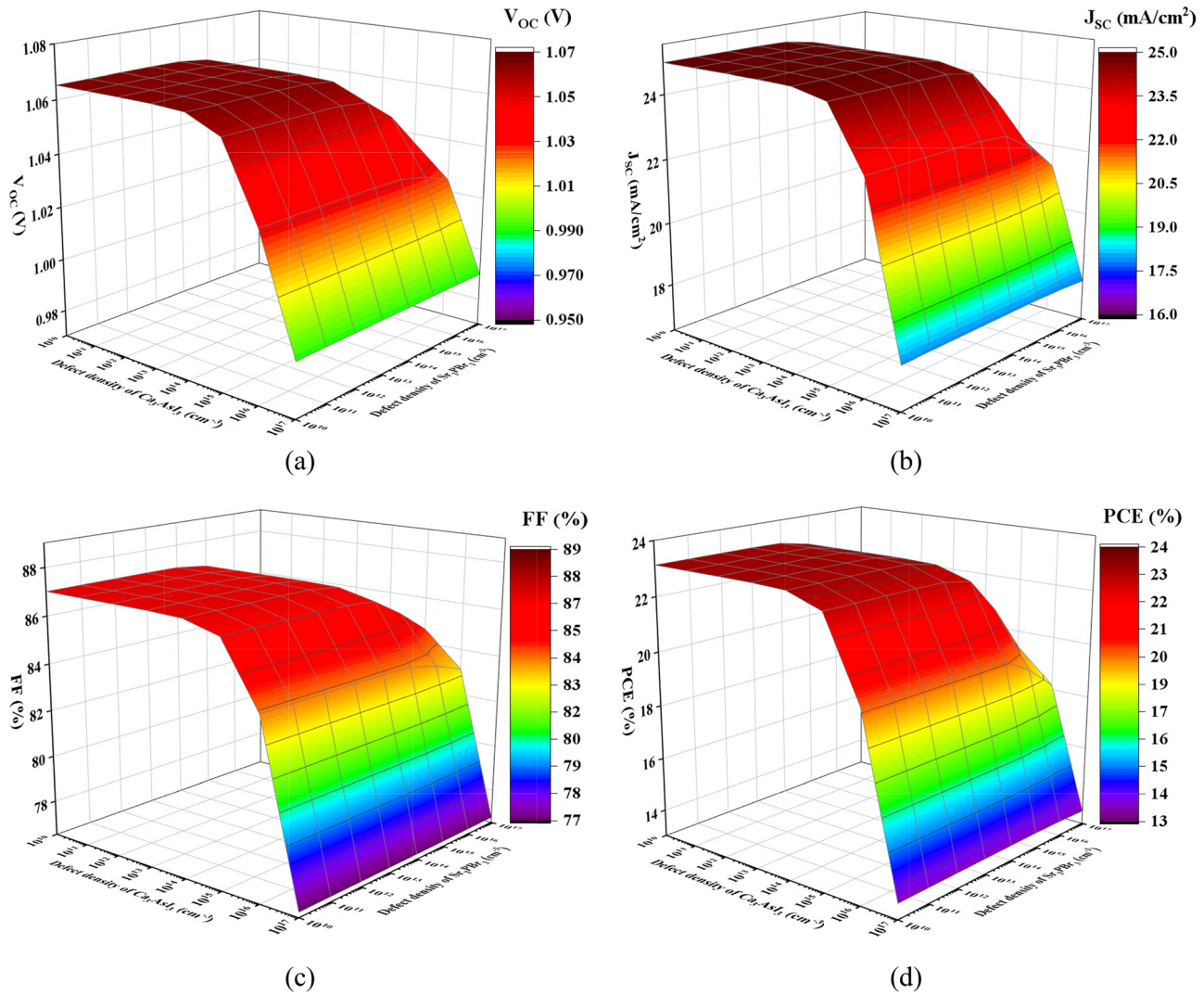

Fig. 6 Role of defect variation in Sr_3PBr_3 and Ca_3AsI_3 (device-iii) on output parameters, (a) V_{OC}, (b) J_{SC}, (c) FF, and (d) PCE.

at 22.61% for a thickness of 3.0 μm for device-i and 21.22% for device-ii. Notable increases are seen up to 2.0 μm before plateauing. Furthermore, the FF increases with thickness, reaching its highest value for device-i at 89.1% and device-ii at 87.8%. The J_{SC} also increases with depth, reaching 23.5 mA for device-i and 22.8 mA for device-ii, respectively at 3.0 μm, suggesting improved light absorption in device-i.[57] For device-i and device-ii, the V_{OC} show little rise and stabilizes at 1.08 V and 1.06 V, respectively. Compared to device-ii, device-i shows superior material qualities and performs better in all categories.

The given contour plots in Fig. 3 show how changing the thickness of Sr_3PbBr_3 and Ca_3AsI_3 affects device-iii photovoltaic performance. According to the results, the output parameters for both the absorber improve with increasing thickness. As thickness increases, V_{OC} increases steadily to approximately 1.089 V. Additionally, J_{SC} improves to 27 mA cm^{-2}, with the highest values observed for thicker Sr_3PbBr_3 layers. For thicker material combinations, the FF also increases, peaking at 88%. PCE values rises from 20.44% to a maximum of 25.62% as a result of the thickness increment. Based on the analysis, it appears that thicker layers of Sr_3PbBr_3 and Ca_3AsI_3 are optimal for photovoltaic efficiency, though practical issues such as fabrication limitations and material costs must also be considered.

The impact of altering the thicknesses of Sr_3PbBr_3 and Ca_3AsI_3 (with HTL) on photovoltaic properties of device-iv is demonstrated in Fig. 4. When the thicknesses of Sr_3PbBr_3 and Ca_3AsI_3 are both around 1 μm, the greatest value of 1.263 V is seen in the contour plot of Fig. 4(a), where V_{OC} varies between 1.200 and 1.300 V. Fig. 4(b) displays J_{SC} values between 26.00 and 28.50 mA cm^{-2}, with a noteworthy value of 27.56 mA cm^{-2} attained when both layers are about 2 μm thick. The FF is shown in Fig. 4(c) and ranges from 85.00% to 88.00%, reaching a maximum of 87.25% at a thickness of 2.5 μm for Sr_3PbBr_3 and 2.0 μm for Ca_3AsI_3. Lastly, Fig. 4(d) shows that when both Sr_3PbBr_3 and Ca_3AsI_3 have a thickness of around 2.5 μm, the PCE achieves a peak of 30.02% owing to generation of more carriers.[58] The optimized thickness of 1 μm for both Sr_3PbBr_3 and Ca_3AsI_3 in the double absorber solar cell is chosen to balance light absorption with minimizing recombination and transport losses. Although increasing the thickness to 2.5 μm results in a peak PCE of 30.02%, the efficiency improvement beyond 1 μm remains marginal, as most incident photons are already absorbed (absorption saturation). The additional thickness primarily enhances carrier recombination, thereby offsetting the potential performance gains. These results indicate that while thicker absorbers can achieve a peak PCE of 30.02%, an optimal thickness of 1 μm best balances absorption and recombination losses.

3.3. Impact of the defect density of the active layers on PV parameters

The Fig. 5 illustrates the influence of defect density in the absorber layer on the performance of two different devices.

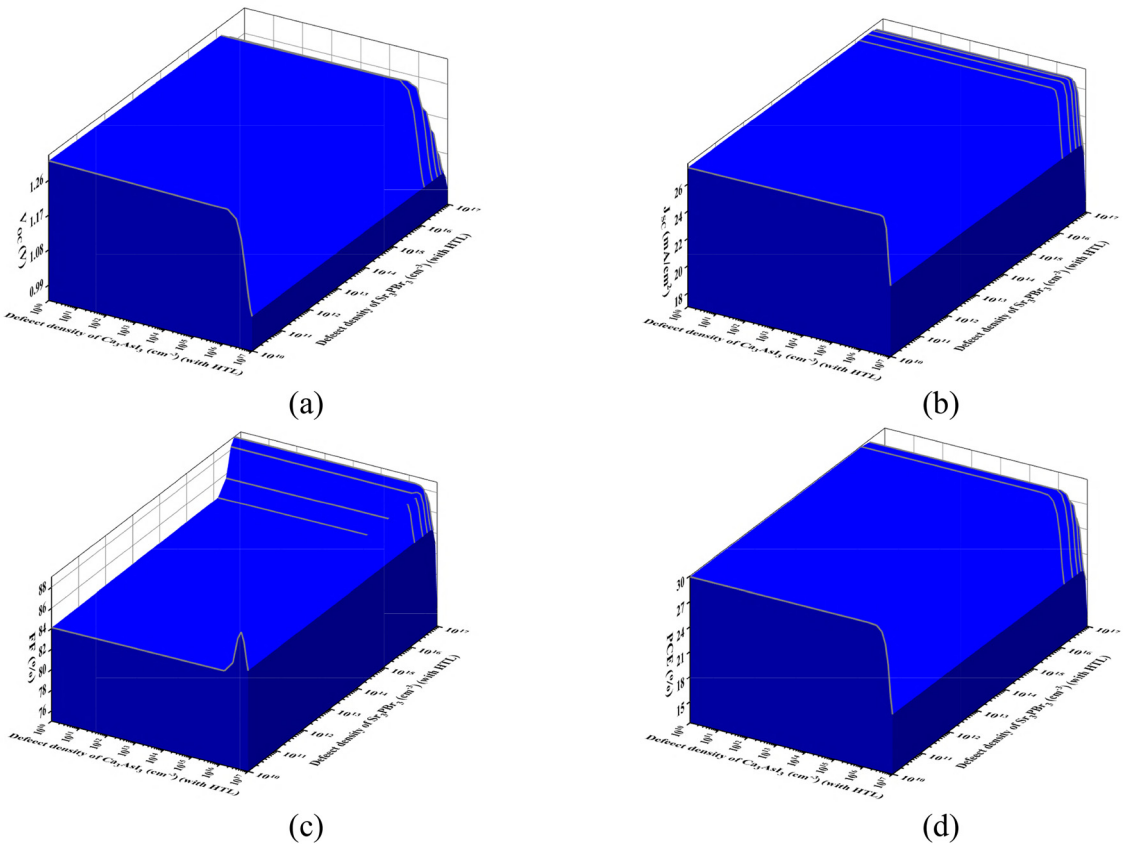

Fig. 7 Impact of defect density variation in Sr_3PBr_3 and Ca_3AsI_3 (device-iv) on the photovoltaic parameters, (a) V_{OC}, (b) J_{SC}, (c) FF, and (d) PCE.

As the defect density increases, both devices show a reduction in key output parameters, including J_{SC}, V_{OC}, and FF, which collectively lead to a decrease in the overall PCE.

For device i, the efficiency decreases from almost 21% at 10^{10} cm^{-3} defect density to less than 15% at the highest defect density of 10^{17} cm^{-3}, while for device ii, a similar trend is observed, with PCE dropping from nearly 20% to approximately 13%. This variation is driven by the increased recombination centres for the charge carriers at higher defect densities,[33] which hinders charge transport and reduces the device's ability to generate and collect photo-generated carriers effectively. The observed decline in performance is a direct consequence of the higher density of traps that impede carrier mobility and reduce the overall efficiency of the photovoltaic conversion process.

The Fig. 6 presents the influence of defect density in the absorber layer on the performance of device iii. As defect density increases, the device's performance deteriorates, as evidenced by a reduction in key output parameters. Specifically, the J_{SC} decreases from 25.0 mA cm^{-2} to 18.0 mA cm^{-2}, the V_{OC} drops from 1.065 V to 0.99 V, and the FF declines from 87% to 71%. Consequently, the PCE decreases from 23.16% to 12.65%. These variations are due to the enhanced recombination of charge carriers at the defect sites within the absorber layer.[59] The increased defect density provides additional recombination centres for both electrons and holes,[33] leading to a reduction in the number of charge carriers available for collection at the electrodes, which in turn decreases the overall device efficiency.[60] The physical mechanism underlying this performance degradation is the increased probability of non-radiative recombination, which results in significant energy loss in the form of heat, thereby diminishing the electrical output of the device.

Fig. 7 highlights the significant influence of defect densities in Sr_3PBr_3 and Ca_3AsI_3 on the performance of device-IV, with particular attention given to key photovoltaic characteristics. The device demonstrates optimal performance at low defect densities ($\leq 10^{15}$ cm^{-3}), achieving a peak PCE of 30%, a J_{SC} of 26.5 mA cm^{-2}, an FF of 88.5%, and a V_{OC} of 1.28 V. However, as the defect density increases to 10^{17} cm^{-3}, all performance metrics experience a significant decline. Specifically, the PCE decreases to 13.54%, the J_{SC} drops to approximately 18 mA cm^{-2}, the FF reduces to around 76%, and the V_{OC} falls to about 0.99 V. These reductions underscore the adverse impact of defects, which lead to heightened recombination losses by obstructing the transport of carrier[61,62] and a substantial decline in the overall efficiency of the device.[63,64] In this case, the defect density of 10^{12} cm^{-3} is chosen as the optimized value to maintain minimal recombination losses, allowing for high photovoltaic efficiency.

3.4. Impact of the acceptor density of the active layers on PV parameters

The Fig. 8 presents the impact of shallow acceptor density in the absorber layer on the performance of two devices: device i, and device ii. For device i, as the shallow acceptor density

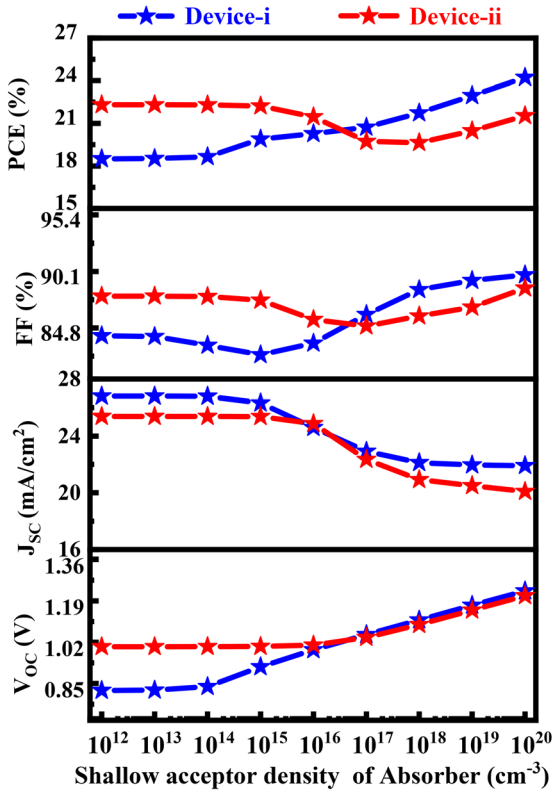

Fig. 8 Effect of doping variation in Sr_3PBr_3 and Ca_3AsI_3 (device-i and device-ii) on the photovoltaic output parameters.

increases from 10^{12} cm^{-3} to 10^{20} cm^{-3}, the PCE increases from nearly 19.20% to almost 24.05%, the J_{SC} decreases from 27 mA cm^{-2} to 22 mA cm^{-2}, the FF rises from 84.7% to 91.1%, and the V_{OC} progressively rises from 0.84 V to around 1.20 V. This enhancement in performance can be arisen from the passivation of deep-level traps by shallow acceptors, which helps to improve carrier mobility and reduce recombination losses resulting in enhanced charge transport and extraction,[65] thus increasing the overall efficiency. On the other hand, for device ii, as the shallow acceptor density increases, the PCE decreases from 22.5% to 19.53% when the shallow acceptor density rises from 10^{12} cm^{-3} to 10^{17} cm^{-3}, the J_{SC} drops from 25.5 mA cm^{-2} to approximately 21.6 mA cm^{-2}, the FF declines from 87.4% to 84.5%, and V_{OC} upsurges from 1.01 V to 1.07 V. In this case, the shallow acceptors likely introduce additional charge carrier traps that facilitate recombination, leading to a loss in efficiency. Beyond the shallow acceptor density of 10^{17} cm^{-3} the PCE raises slightly. The contrasting behaviors in the two devices may be due to differences in material properties and defect tolerance. While shallow acceptors can passivate certain types of defects in Sr_3PBr_3 (used in device i), they may worsen the defect landscape in Ca_3AsI_3 (used in device ii), highlighting the material-specific impact of defect engineering on device performance. In summary, For device-i, PCE peaks at $\sim$24.05% when the shallow acceptor density is 10^{20} cm^{-3} due to trap passivation, while device-ii achieves its maximum ($\sim$22.5%) at 10^{12} cm^{-3}.

The effect of shallow acceptor density (N_A) in Sr_3PBr_3 and Ca_3AsI_3 of device-iii on key photovoltaic parameters is illustrated in Fig. 9. In low densities (10^{12} cm^{-3}), V_{OC} has started at approximately 0.80 V and increases to 1.21 V at higher densities (10^{19} cm^{-3}). On the other hand, J_{SC} peaks at about 28 mA cm^{-2} when N_A is less than 10^{14} cm^{-3} for both the absorber. With higher doping levels, the FF improves from around 77% at low acceptor densities to a maximum of 88% at high acceptor densities. PCE also follows a similar trend, beginning at roughly 15% at low N_A values and rising to 28% with increasing acceptor density. Overall, device-iii attains its highest PCE (~28%) at shallow acceptor densities near 10^{19} cm^{-3}. The positive correlation between N_A and efficiency can be linked to the increased density of states that facilitate hole transport and enhance charge carrier collection efficiency. The higher concentration of shallow acceptors helps to better balance the electron–hole pairs within the absorber layer, reducing recombination losses and improving the overall photovoltaic efficiency.

The evaluation of the impact of doping variation on photovoltaic parameters in Sr_3PbBr_3 and Ca_3AsI_3 (device-IV) with a HTL is depicted in Fig. 10. As the acceptor densities of the materials increase from 10^{13} cm^{-3} to 10^{20} cm^{-3}, the V_{OC} rises from 1.27 V to 1.34 V, demonstrating a significant dependence on the shallow acceptor densities. This behavior results from the enhanced hole concentration at higher acceptor doping levels, which suppresses charge-carrier recombination and strengthens the built-in electric field,[65] thus leading to higher V_{OC}. To optimize voltage performance, it is essential to achieve an optimal doping level, particularly for acceptor densities exceeding 10^{18} cm^{-3}. The J_{SC}, however, remains largely unaffected across the doping range, indicating that it is less sensitive to variations in acceptor density, particularly when the doping concentration exceeds 10^{17} cm^{-3}. This can be explained by the fact that J_{SC} is more dependent on the light absorption and the generation of charge carriers than on the doping levels, once a sufficient concentration of free carriers is established within the material. The FF, which varies between

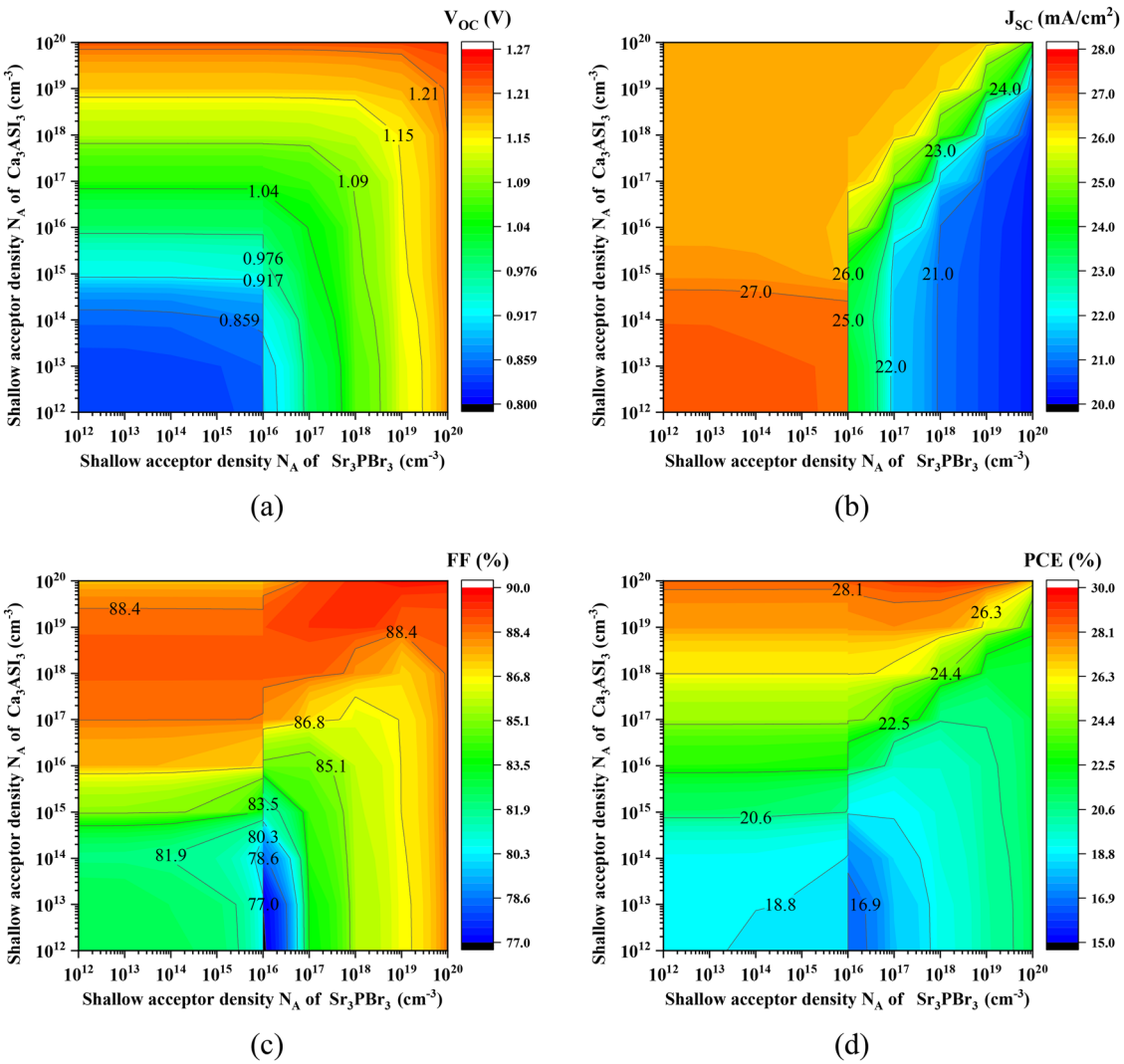

Fig. 9 Role of shallow acceptor density variation in Sr_3PBr_3 and Ca_3AsI_3 (device-iii) on the photovoltaic parameters, (a) V_{OC}, (b) J_{SC}, (c) FF, and (d) PCE.

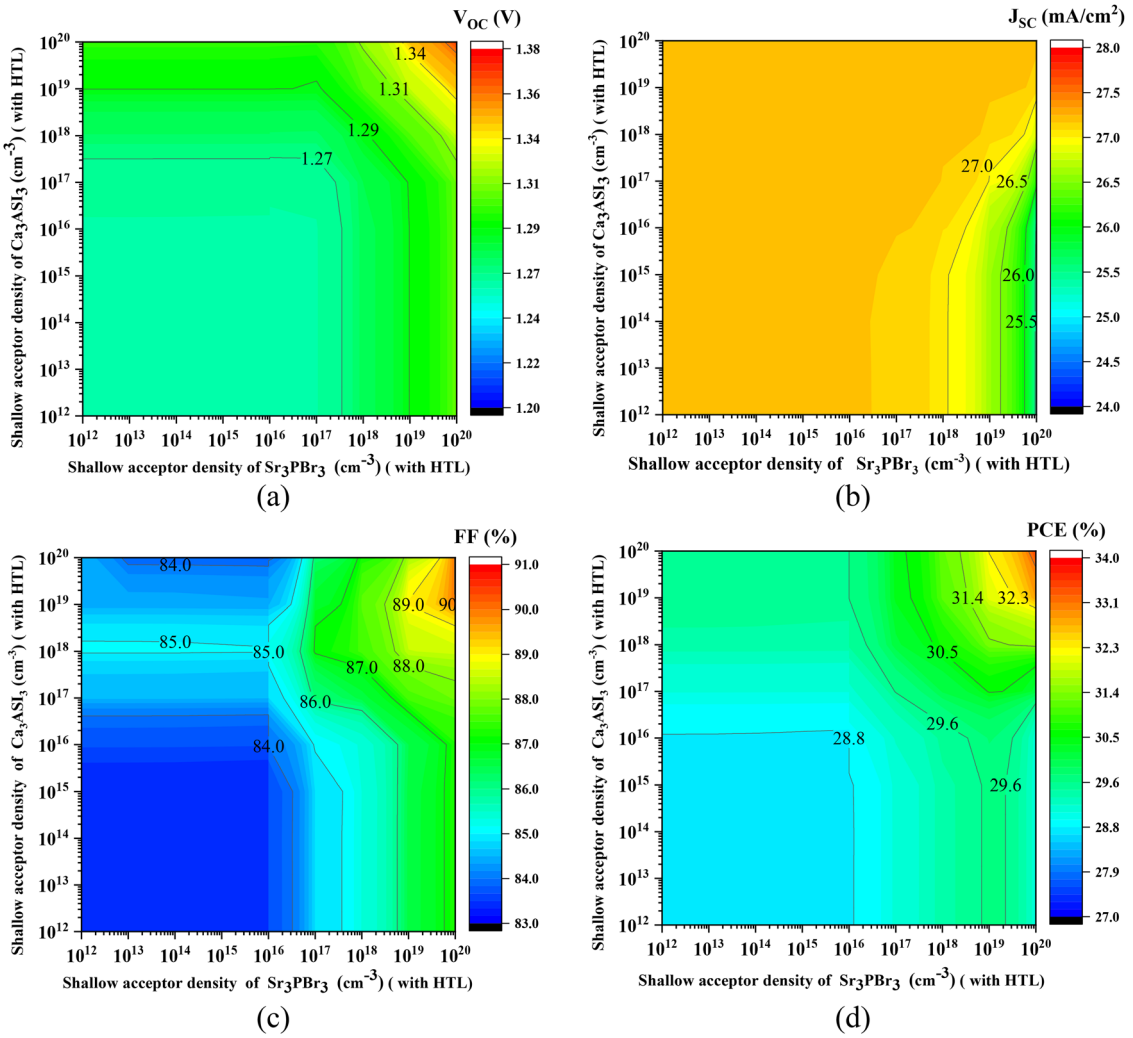

Fig. 10 The effect of doping variation in Sr_3PBr_3 and Ca_3AsI_3 with HTL (device-iv) on the output of PSC, (a) V_{OC}, (b) J_{SC}, (c) FF, and (d) PCE.

84% and 91%, improves with increased doping, reflecting the enhanced device performance at higher acceptor densities above 10^{17} cm^{-3}. This increase in FF can be owing to reduced series resistance and enhanced charge transport efficiency, which lead to better extraction of charge carriers and more effective utilization of the photo-generated current. Furthermore, higher acceptor densities result in an increase in PCE, ranging from 29.6% to 32.3%. This improvement is a consequence of the combined effects of higher V_{OC} and FF, which collectively enhance the overall PCE of the device. The overall trend indicates that shallow acceptor densities of 10^{18} cm^{-3} for Sr_3PbBr_3 and 10^{17} cm^{-3} for Ca_3AsI_3 are optimal for device IV, yielding a peak PCE of ~32.3%, a V_{OC} of 1.34 V, and an FF of ~91%

3.5. Influence of the interface defect density on PV parameters

Fig. 11 depicts the impact of interface defect density, ranging from 10^9 to 10^{16} cm^{-2}, on the photovoltaic parameters of Sr_3PBr_3/CdS, Sr_3PBr_3/Ca_3AsI_3, MoO_3/Sr_3PBr_3, and Ca_3AsI_3/CdS interfaces. As defect density increases, the PCE decreases across all interfaces. Specifically, the MoO_3/Sr_3PbBr_3 interface, with an initial defect density of 10^9 cm^{-2}, shows the highest initial PCE of 28.5%, and it remains relatively stable, decreasing only to 24% at a defect density of 10^{16} cm^{-2}. In contrast, the Ca_3AsI_3/CdS interface experiences a significant decline in PCE, from 19% to approximately 11%. This decrease in efficiency can be resulting from the increased carrier recombination at the defect sites,[66,67] which serve as traps for charge carriers, reducing the number of free carriers available for photovoltaic conversion. For most interfaces, the FF remains stable at first but then decreases with increasing defect density.

To mitigate interface-related recombination losses, several fabrication strategies can be employed. Interface passivation using ultrathin dielectric layers (*e.g.*, Al_2O_3, MgO) or self-assembled organic monolayers can reduce defect density and suppress nonradiative recombination. Compositional grading at the absorber/transport layer junction can improve band alignment and carrier selectivity, while optimized low-temperature deposition or post-deposition annealing can minimize

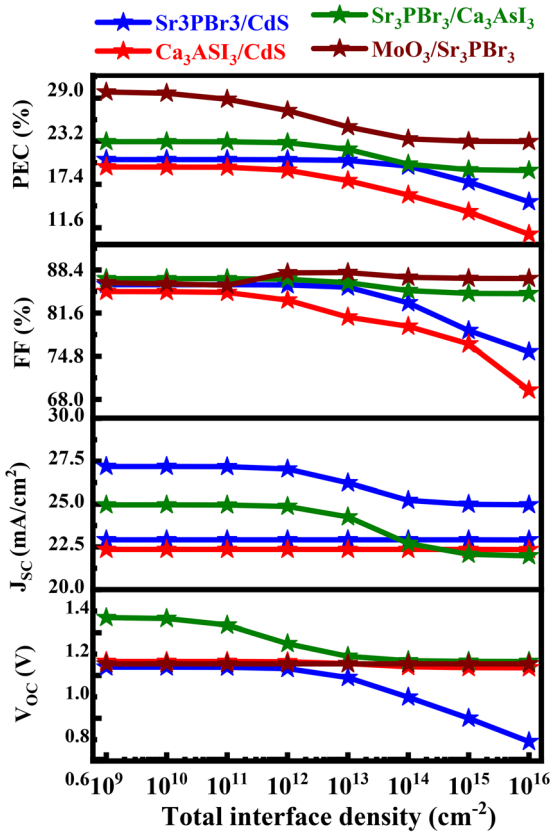

Fig. 11 Effect of interface defect density on PV solar cell.

defect formation without damaging underlying layers. Implementing such approaches during fabrication could significantly enhance device performance and stability by reducing the detrimental effects of interface defects.

However, for the MoO_3/Sr_3PbBr_3 interface the device demonstrates remarkable stability, maintaining an FF of 88% across the entire defect density range. This could be due to better charge transport properties and fewer resistive losses at the interface, even with increased defects. The J_{SC} shows a slight decline in the Sr_3PbBr_3/CdS and Sr_3PbBr_3/Ca_3AsI_3 interfaces, with J_{SC} dropping from 27.5 mA cm^{-2} to 25 mA cm^{-2} and from 25 mA cm^{-2} to 21 mA cm^{-2}, respectively. The reduction in J_{SC} is occurring due to the increased recombination of charge carriers at the defect sites, which lowers the number of photogenerated carriers that contribute to the current. However, for the MoO_3/Sr_3PbBr_3 interface, J_{SC} remains constant at 27 mA cm^{-2}, suggesting that the interface maintains efficient charge collection despite an increase in defect density. The V_{OC} shows a steep drop for the Sr_3PbBr_3/CdS interface, from nearly 1.2 V to around 0.8 V, due to the increased carrier recombination at the defect sites, which reduces the built-in potential. On the other hand, the MoO_3/Sr_3PbBr_3 interface exhibits higher stability, with V_{OC} remaining at approximately 1.1 V even at high defect concentrations. This suggests that the MoO_3/Sr_3PbBr_3 interface possesses superior performance stability, likely due to better defect passivation or reduced impact of defects on the overall charge carrier dynamics.

3.6. Impact of temperature

Fig. 12 illustrates the effects of temperature on the performance of four photovoltaic devices (device-i, device-ii, device-iii, and device-iv). A general decrease in PCE is observed across all devices with temperature variation from 275 K and 475 K. For example, device-i shows a significant drop in efficiency, decreasing from approximately 22% at 275 K to 12% at 475 K. In contrast, device-iv demonstrates better thermal stability, with a more moderate decline from about 29% to 23%. This reduction in PCE with increasing temperature can be a consequence of the increased recombination rates of charge carriers at higher temperatures,[68] which reduce the number of free charge carriers available for power generation, thus diminishing the overall efficiency. The FF also decreases steadily with temperature, ranging from 88% at 275 K to nearly 80% at 475 K. This decline in FF is a result of increased resistive losses, including both series resistance and shunt resistance, as the temperature rises.[69] The increased thermal agitation of charge carriers at higher temperatures leads to greater scattering, resulting in higher resistance within the device and consequently, a reduced FF. Notably, device-iv maintains relatively higher FF values compared to the other devices, suggesting its superior ability to mitigate these thermal losses. Regarding J_{SC}, most devices (device-i, device-iii, and device-iv) show little variation with increasing temperature. This stability suggests that the generation of charge carriers under illumination is less

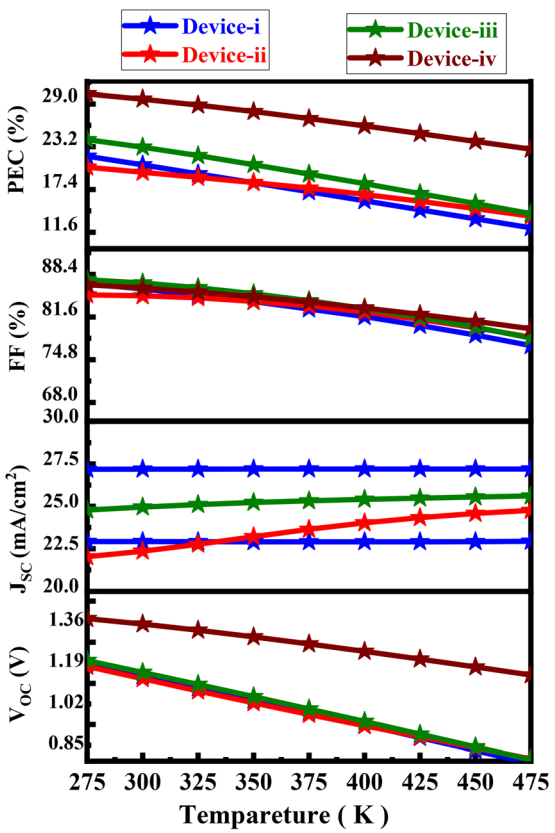

Fig. 12 Effect of temperature change on PV solar cell.

sensitive to temperature changes, likely due to a balance between the enhanced carrier mobility at higher temperatures and the increased recombination rates. However, device-ii exhibits a marginal improvement in J_{SC} with temperature, increasing from about 21.5 mA cm^{-2} at 275 K to approximately 24.5 mA cm^{-2} at 475 K. This can be explained by the fact that in some materials, increased temperature can lead to higher carrier mobility and improved charge collection, resulting in a slight increase in J_{SC}. Finally, the V_{OC} decreases for all devices as the temperature increases from 275 K to 475 K. This behavior is associated with the negative temperature coefficient of the bandgap, which causes the V_{OC} to decline as the temperature increases. In particular, device-iv exhibits lower sensitivity to temperature changes, with V_{OC} declining from about 1.36 V at 275 K to 1.18 V at 475 K. This lower sensitivity suggests that device-iv may have a more favorable material composition or device architecture, which mitigates the detrimental effects of temperature on V_{OC} to a greater extent than the other devices. Overall, device iv sustains a PCE of ~23% at 475 K compared to ~29% at 275 K, demonstrating superior thermal stability relative to other devices, whose efficiencies fall below 20% at elevated temperatures.

Fig. 13 displays data comparing the total generation rates, recombination rates, and carrier concentrations of four devices. All of the devices in the active region have a constant high total generation rate (~10^{22} cm^{-3} s^{-1}) in Fig. 13(a). However, they show a sudden increase close to the interface (~0.2 μm) before stabilizing. The entire recombination rate is shown in Fig. 13(b), with device-ii exhibiting the maximum recombination near the top surface (~10^{16} cm^{-3} s^{-1}). The concentrations of holes and electrons are depicted in Fig. 13(c) and (d), respectively.

Across the solar cell, device-iv has the maximum hole concentration (~10^{18} cm^{-3}), whereas device-i and device-ii have significantly lower values. Comparably, device-iv retains a peak value of ~10^{23} cm^{-3} close to the bottom surface (~2.1 μm) for electron concentration (Fig. 13(d)), whereas device-i and device-ii have lesser concentrations (~10^{17} cm^{-3}). With lower recombination losses and better carrier production and retention, these results show that device-iv has the potential

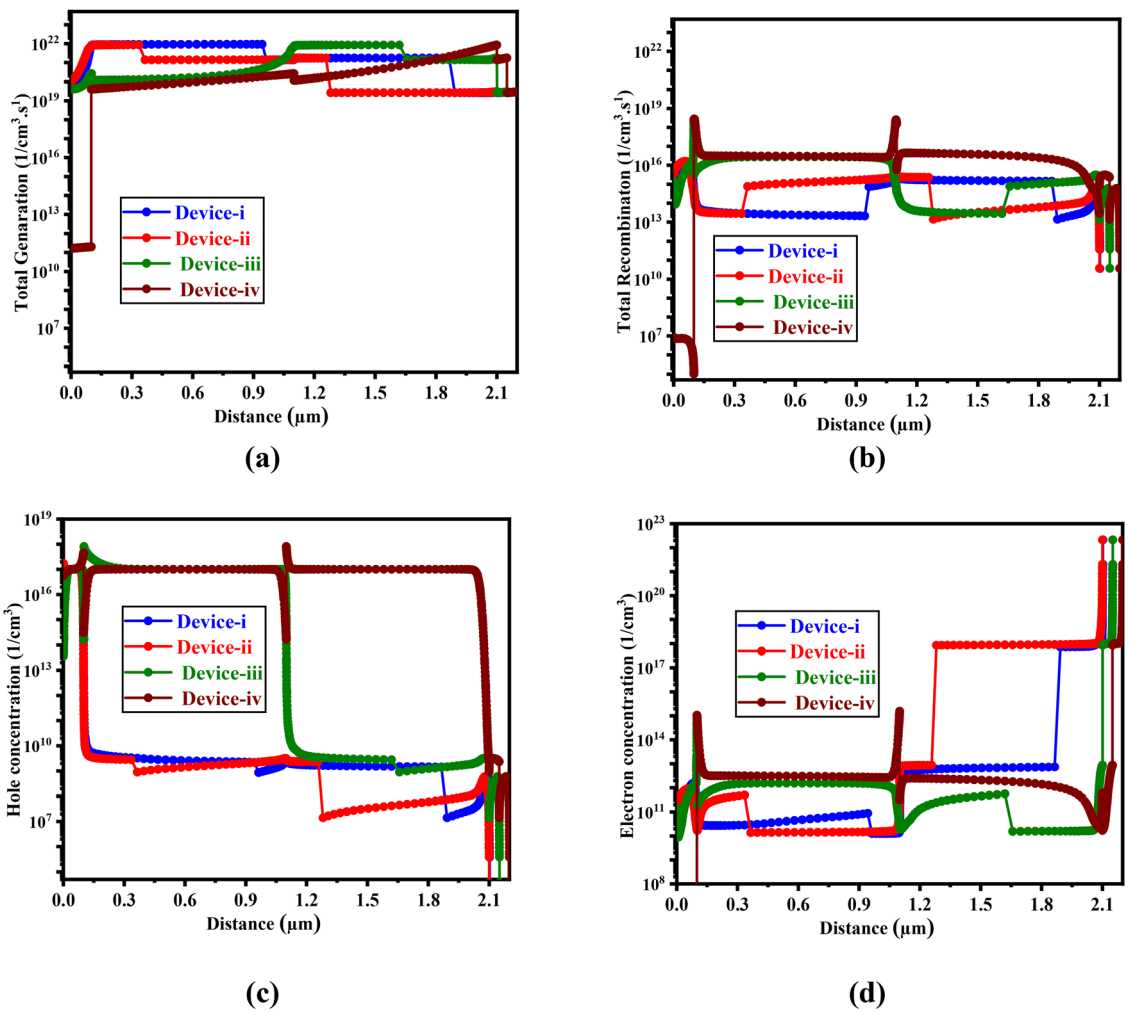

Fig. 13 The (a) total generation rate, (b) total recombination rate, (c) hole concentration, and (d) electron concentration across the investigated optimized devices.

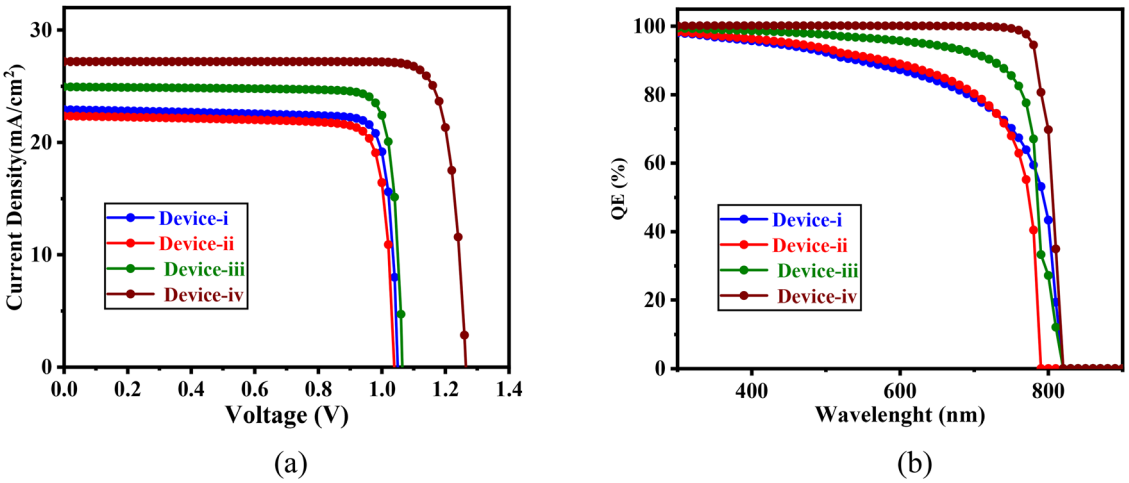

Fig. 14 (a) *J–V* and (b) QE curves of the PSC for the best-optimized structure, device-i, device-ii, device-iii and device-iv.

Table 3 Obtained output parameters of the PSCs of this work

Devices	V_{OC} (V)	J_{SC} (mA cm^{-2})	FF (%)	PCE (%) (Ave. ± Dev.)
Device-i (FTO/CdS/Sr_3PBr_3/Au)	1.05	22.92	86.06	20.71 ± 0.05
Device-ii (FTO/CdS/Ca_3AsI_3/Au)	1.04	22.35	84.97	19.75 ± 0.06
Device-iii (FTO/CdS/Ca_3AsI_3/Sr_3PBr_3/Au)	1.07	24.95	87.02	23.23 ± 0.04
Device-iv (FTO/CdS/Ca_3AsI_3/Sr_3PBr_3/MoO_3/Au)	1.27	27.19	86.20	29.77 ± 0.03

to be a more efficient device. In summary, device iv exhibits a peak hole concentration of $\sim 10^{18}$ cm^{-3} and an electron concentration of $\sim 10^{23}$ cm^{-3} near the back contact, with recombination rates significantly lower than those in single-absorber devices.

3.7. *J–V* & QE characteristics

A comparison of the *J–V* and QE characteristics of four PSCs using the optimized parameters is depicted in Fig. 14. The *J–V* characteristics of the devices in Fig. 14(a) indicate that device iv exhibits the highest performance, which can be facilitated by several factors. This device benefits from the MoO_3 HTL, which improves hole extraction and reduces recombination losses, thereby enhancing the J_{SC} and overall efficiency. The dual perovskite absorbers, Ca_3AsI_3 and Sr_3PBr_3, also contribute to a broad absorption spectrum,[70] allowing for better light harvesting, particularly in the visible to near-infrared regions. This results in a high J_{SC} and V_{OC}, translating into superior overall efficiency.[33] Device iii shows a slightly lower performance, likely due to a lack of HTL, which could hinder charge collection. Device i also shows good performance but suffers from a lack of the complementary absorber layer, reducing the absorption range. Device ii exhibits the lowest performance, primarily due to the instability of Ca_3AsI_3 and poor charge transport at the interfaces.

The QE curves of Fig. 14(b) shows that device iv exhibits the highest performance, particularly across a broad spectral range, several factors might be responsible for this. The dual perovskite absorbers of Ca_3AsI_3 and Sr_3PBr_3 is offered complementary absorption properties, enhancing light harvesting efficiency and leading to high QE in the visible and near-infrared regions. The inclusion of MoO_3 as a HTL improves hole extraction, reduces recombination losses, and contributes to a higher J_{SC}, which is crucial for the enhanced performance seen in the *J–V* characteristics. Device iii shows good QE, but the absence of MoO_3 and potential interface issues between the two perovskites lead to slightly lower performance compared to device iv. Device i exhibits strong QE but lacks the additional Ca_3AsI_3 layer, reducing its absorption range, particularly at longer wavelengths. Device ii shows the lowest QE, especially at longer wavelengths, due to the limited absorption properties of Ca_3AsI_3 and potential recombination effect,[71] leading to poor charge transport. Consequently, device iv attains a V_{OC} of 1.27 V, a J_{SC} of 27.19 mA cm^{-2}, an FF of 86.20%, and a PCE of 29.77%, along with the broadest QE response, confirming the synergistic advantages of the dual absorbers and the MoO_3 HTL.

Table 3 presents a comparison of the output parameters for four device configurations. Device iv exhibits the highest performance, benefiting from the use of an HTL. Device iii shows a decline in performance, indicating reduced transport efficiency due to the absence of the HTL. Device i demonstrates further performance degradation, likely caused by reduced charge generation from utilizing only a single absorber layer. Finally, device ii achieves the lowest PCE, a result of significant reduction in carrier generation.

4. Conclusions

The findings of this study reveal that the photovoltaic efficiency of PSCs is significantly affected by key parameters such as

absorber material choice, layer thickness, defect concentration, and interface properties. Of the configurations examined, device-iv-featuring dual absorbers (Ca_3AsI_3 and Sr_3PBr_3) along with MoO_3 HTL achieved the highest power conversion efficiency of 29.77%. This superior performance is originating from the improved light harvesting, minimized recombination losses, and effective charge extraction. The results highlight that fine-tuning absorber thickness and controlling defect density are critical for optimizing efficiency. From a fabrication perspective, the proposed Ca_3AsI_3/Sr_3PBr_3 dual-absorber architecture is compatible with established thin-film deposition techniques such as sequential thermal evaporation, co-evaporation, or solution-based layer-by-layer processing, which allow precise control over thickness and composition. MoO_3 HTL integration is feasible *via* low-temperature thermal evaporation or spin coating, ensuring minimal thermal stress on underlying layers. Both absorbers exhibit thermal stability suitable for ambient or low-temperature processing, and their band alignment requirements can be met through controlled deposition rates and post-deposition annealing. These factors indicate that the simulated device structure is amenable to experimental realization using scalable fabrication routes. Additionally, temperature-dependent studies demonstrated that device-iv maintained greater thermal stability compared to the other designs, indicating strong potential for practical deployment. Overall, the study underscores the vital role of material and structural optimization in enhancing PSC performance, and it points to the promise of multi-absorber systems and interface engineering in advancing next-generation, high-efficiency solar technologies.

Conflicts of interest

There are no conflicts to declare.

Data availability

Data will be available on request.

Acknowledgements

A. Irfan extends his appreciation to the Deanship of Research and Graduate Studies at King Khalid University for funding this work through the Large Groups Research Project under grant number (RGP2/74/46). Authors are thankful to the Deanship of Graduate Studies and Scientific Research at the University of Bisha for supporting this work through the Fast-Track Research Support Program.

References

1 J. Al Mahmud, M. F. Rahman, A. Kuddus, M. H. Ali, A. T. M. S. Islam, M. D. Haque, S. R. Al Ahmed, M. Mushtaq and A. B. M. Ismail, Design and analysis of a SnS2/WS2/V2O5 double-heterojunction toward high-performance photovoltaics, *Energy Adv.*, 2023, **2**, 1843–1858.
2 T. Y. Tang, X. H. Zhao, D. Y. Hu, Q. Q. Liang, X. N. Wei and Y. L. Tang, Theoretical exploration of mechanical, electronic structure and optical properties of aluminium based double halide perovskite, *RSC Adv.*, 2022, **12**, 10209–10218.
3 M. F. Rahman, M. H. Rahman, A. Kuddus, A. R. Chaudhry and A. Irfan, Unveiling the Structural, Electronic, Optical, Mechanical, and Photovoltaic Properties of Lead-Free Inorganic New Ba3MBr3 (M = As, N, P, and Sb) Perovskites, *Energy Fuels*, 2024, **38**, 7260–7278.
4 S. S. Ahamdi and P. Amiri, Stability, electronic, thermodynamic, and optical aspects of CsPbI3-xBrx(x = 0, 1, 2, 3) compounds: An ab-initio study, *Solid State Commun.*, 2023, **372**, 115304.
5 H. J. Snaith, Perovskites: the emergence of a new era for low-cost, high-efficiency solar cells, *J. Phys. Chem. Lett.*, 2013, **4**, 3623–3630.
6 F. Rayhan, M. H. Rahman, S. Rana, D. Das Ria, J. I. Chy, M. S. Hosen, T. Ahamed, J. Sarpong, K. Yegbe and M. S. Uddin, Unveiling the potential of non-toxic Ge based perovskite material for all inorganic solar cells using multiple ETLs, *Photonics Nanostruct. Fundam. Appl.*, 2025, **66**, 101425.
7 M. K. Hossain, S. Islam, M. S. Uddin, P. Kanjariya, A. Rajiv, A. Shankhyan, H. M. Albert, A. S. M. Metwally and R. Haldhar, An in-depth study on charge transport layers for designing and optimizing high-efficiency lead-free CsSnGeI3-based double-perovskite solar cells: A numerical approach, *J. Phys. Chem. Solids*, 2025, **203**, 112715.
8 K. Sidra, S. Yadav, V. Chakraborty, J. Singh, R. Singh, M. Hasnain and S. M. Hasnain, Perovskite solar cell's Efficiency, Stability and Scalability: A Review, *Mater. Sci. Energy Technol.*, 2023, **6**, 437–459.
9 A. Paul, B. Sarkar, S. Paul, A. Moyez, H. Jung and S. Roy, *Encyclopedia of Materials: Electronics*, 2023, **1**, 418–433.
10 A. R. Chourasia, S. Islam, E. Aloyine and P. Adhikari, Oxidation of cobalt as investigated by x-ray photoelectron spectroscopy, *Surf. Sci. Spectra*, 2024, **31**, 14008.
11 H. Bencherif and M. Khalid Hossain, Design and numerical investigation of efficient (FAPbI3)1−x(CsSnI3)x perovskite solar cell with optimized performances, *Sol. Energy*, 2022, **248**, 137–148.
12 H. Bencherif, F. Meddour, M. H. Elshorbagy, M. Khalid Hossain, A. Cuadrado, M. A. Abdi, T. Bendib, S. Kouda and J. Alda, Performance enhancement of (FAPbI3)1-x(MAPbBr3)x perovskite solar cell with an optimized design, *Micro Nanostruct.*, 2022, **171**, 207403.
13 K. M. Sadat, M. K. Hossain, M. S. Uddin, P. Prabhu, A. Aggarwal, K. Gopalakrishna, P. S. Kiran, A. K. Mishra, S. K. Shah, S. Islam, A. M. S. Alhuthali, M. H. Abdellattif and V. K. Mishra, Exploration and optimization of different charge transport layers for Cs4CuSb2Cl12 based perovskite solar cells, *Sci. Rep.*, 2025, **15**, 25100.
14 M. A. Islam, M. K. Hossain, M. S. Uddin, A. K. Datta, S. Islam, P. S. Bains, R. Sharma, A. Rajiv, A. M. S.

Alhuthali, M. H. Abdellattif, D. K. Dwivedi and R. Haldhar, Design and simulation of the potential of lead-free Ag 3 Bi 1.1 I 6.3 perovskite solar cells with different charge transport for energy enhancement, *RSC Adv.*, 2025, **15**, 27558–27575.

15 M. Ferdous Rahman, P. Barman, M. Azizur Rahman, M. Mushtaq, M. Rasidul Islam, M. Atikur Rahman, M. Z. Sultan, A. R. Chaudhry and A. Irfan, Electronic, optical, thermophysical, and mechanical properties of lead-free Ba3SbBr3 perovskite, *Polyhedron*, 2024, **254**, 116937.

16 M. F. Rahman, M. A. Rahman, M. R. Islam, A. Ghosh, M. A. Bashar Shanto, M. Chowdhury, M. Al Ijajul Islam, M. H. Rahman, M. K. Hossain and M. A. Islam, Unraveling the strain-induced and spin-orbit coupling effect of novel inorganic halide perovskites of Ca3AsI3 using DFT, *AIP Adv.*, 2023, **13**, 085329.

17 J. Y. Kim, J.-W. Lee, H. S. Jung, H. Shin and N.-G. Park, High-Efficiency Perovskite Solar Cells, *Chem. Rev.*, 2020, **120**, 7867–7918.

18 N. Suresh Kumar and K. Chandra Babu Naidu, A review on perovskite solar cells (PSCs), materials and applications, *J. Mater.*, 2021, **7**, 940–956.

19 A. Kojima, K. Teshima, Y. Shirai and T. Miyasaka, Organometal halide perovskites as visible-light sensitizers for photovoltaic cells, *J. Am. Chem. Soc.*, 2009, **131**, 6050–6051.

20 A. Ghosh, M. Ferdous Rahman, A. Kuddus, M. K. A. Mohammed, M. Rasidul Islam, S. Bhattarai, A. R. Chaudhry and A. Irfan, Investigating of novel inorganic cubic perovskites of A3BX3 (A = Ca, Sr, B[dbnd]P, As, X = I, Br) and their photovoltaic performance with efficiency over 28%, *J. Alloys Compd.*, 2024, **986**, 174097.

21 M. F. Rahman, M. A. Rahman, R. Rahaman, M. S. H. Choudhury, M. Z. Hasan, A. R. Chaudhry and A. Irfan, Investigation of structural, electronic, optical, mechanical, and solar cell performance of inorganic novel Ca3AsI3 compound through DFT and SCAPS-1D, *Mater. Sci. Eng. B*, 2024, **308**, 117606.

22 S. Islam, D. Das Ria, M. Masum Mia, M. K. A. Mohammed, M. F. Hossain, A. Irfan, N. Dhahri and M. F. Rahman, Introducing a New and Highly Efficient Double-Absorber Solar Cell with Combination of Sr3PBr3 and CsPbI3 Perovskites, *Phys. Status Solidi A*, 2025, 2500148.

23 T. A. Chowdhury, M. A. Bin Zafar, M. Sajjad-Ul Islam, M. Shahinuzzaman, M. A. Islam and M. U. Khandaker, Stability of perovskite solar cells: issues and prospects, *RSC Adv.*, 2023, **13**, 1787–1810.

24 A. Ghosh, F. Ahmed, M. J. Ferdous, M. M. J. Juhi, M. F. I. Buian, A. A. Miazee, M. Sajid, M. Maniruzzaman, A. M. Tighezza, M. F. Ahmmed and M. S. Islam, Strain-induced changes in the electronic, optical and mechanical properties of the inorganic cubic halide perovskite Sr3PBr3 with FP-DFT, *J. Phys. Chem. Solids*, 2024, **191**, 112053.

25 M. S. Rahman, A. K. Datta, S. Islam, M. M. Hasan, U. Das, M. A. Sayed, M. F. Wahid, A. Ghosh and D. Das Ria, Insights from computational analysis on novel Lead-Free FrGeCl3 perovskite solar cell using DFT and SCAPS-1D, *Inorg. Chem. Commun.*, 2024, 113578.

26 J. A. Christians, J. S. Manser and P. V. Kamat, Best Practices in Perovskite Solar Cell Efficiency Measurements. Avoiding the Error of Making Bad Cells Look Good, *J. Phys. Chem. Lett.*, 2015, **6**, 852–857.

27 M. S. Reza, A. Ghosh, N. Drissi, H. Al-Dmour, R. K. Prodhan, M. M. Islam, S. Begum, M. S. Reza and S. Sultana, Evaluation of design and device parameters for lead-free Sr3PBr3/Sr3NCl3 duel-layer perovskite photovoltaic device technology, *RSC Adv.*, 2024, **14**, 36675–36697.

28 M. S. Reza, A. Ghosh, M. S. Reza, S. N. Wornob and S. Sultana, Design and efficiency improvement of eco-conscious Sr3PBr3 and Sr3NCl3 double perovskite solar cells with IGZO and Cu2O as ETL and HTL, *Energy Nexus*, 2025, **18**, 100417.

29 A. Polman, M. Knight, E. C. Garnett, B. Ehrler and W. C. Sinke, Photovoltaic materials: Present efficiencies and future challenges, *Science*, 2016, **352**, DOI: **10.1126/science.aad4424**.

30 I. E. Tinedert, A. Saadoune and M. K. Hossain, A theoretical study of all-inorganic perovskite solar cells: Computational modeling of the CsPbI3/RbGeI3 bilayer absorber structure, *J. Phys. Chem. Solids*, 2024, **189**, 111951.

31 Y. N. Zhang, B. Li, L. Fu, Y. Zou, Q. Li and L. W. Yin, Enhanced optical absorption and efficient cascade electron extraction based on energy band alignment double absorbers perovskite solar cells, *Sol. Energy Mater. Sol. Cells*, 2019, **194**, 168–176.

32 A. Hajjiah, M. Gamal, I. Kandas, N. E. Gorji and N. Shehata, *Sol. Energy Mater. Sol. Cells*, 2022, **248**, 112026.

33 S. Khatoon, V. Chakraborty, S. K. Yadav, S. Diwakar, J. Singh and R. B. Singh, Simulation study of CsPbIxBr1-x and MAPbI3 heterojunction solar cell using SCAPS-1D, *Sol. Energy*, 2023, **254**, 137–157.

34 S. Khatoon, S. K. Yadav, J. Singh and R. B. Singh, Design of a CH3NH3PbI3/CsPbI3-based bilayer solar cell using device simulation, *Heliyon*, 2022, **8**, e09941.

35 S. Bhattarai, M. K. Hossain, R. Pandey, J. Madan, D. P. Samajdar, M. F. Rahman, M. Z. Ansari and M. Amami, Perovskite Solar Cells with Dual Light Absorber Layers for Performance Efficiency Exceeding 30%, *Energy Fuels*, 2023, **37**, 10631–10641.

36 J. Song, C. Huang, X. Zhan, T. Ding, L. Li, Y. Xue, X. Lin, X. Peng, H. Cai, P. Duan and C. Chen, Annealing-Insensitive, Alcohol-Processed MoO x Hole Transport Layer for Universally Enabling High-Performance Conventional and Inverted Organic Solar Cells, *ACS Appl. Mater. Interfaces*, 2022, **14**, 40851–40861.

37 W. Marchal, I. Verboven, J. Kesters, B. Moeremans, C. De Dobbelaere, G. Bonneux, K. Elen, B. Conings, W. Maes, H. G. Boyen, W. Deferme, M. Van Bael and A. Hardy, Steering the properties of MoOx hole transporting layers in OPVs and OLEDs: Interface morphology vs. electronic structure, *Materials*, 2017, **10**, 1–17.

38 J. W. Ma, Z. Liang, C. Jin, X. Y. Jiang and Z. L. Zhang, Enhanced power efficiency for white OLED with MoO3 as hole injection layer and optimized charge balance, *Solid State Commun.*, 2009, **149**, 214–217.

39 C. Girotto, E. Voroshazi, D. Cheyns, P. Heremans and B. P. Rand, Solution-processed MoO 3 thin films as a hole-injection layer for organic solar cells, *ACS Appl. Mater. Interfaces*, 2011, **3**, 3244–3247.
40 M. Burgelman, P. Nollet and S. Degrave, Modelling polycrystalline semiconductor solar cells, *Thin Solid Films*, 2000, **361–362**, 527–532.
41 M. M. Rahman, M. H. Ali, M. D. Haque and A. Z. M. Touhidul Islam, Numerical modeling and extensive analysis of an extremely efficient RbGeI $_3$ -based perovskite solar cell by incorporating a variety of ETL and HTL materials to enhance PV performance, *Energy Adv.*, 2024, **3**, 2377–2398.
42 M. K. Hossain, S. Islam, M. N. Sakib, M. S. Uddin, G. F. I. Toki, M. H. K. Rubel, J. Nasrin, S. H. Shahatha, M. R. Mohammad, A. A. Alothman, C. J. Raorane, R. Haldhar and H. Bencherif, Exploring the Optoelectronic and Photovoltaic Characteristics of Lead-Free Cs2TiBr6 Double Perovskite Solar Cells: A DFT and SCAPS-1D Investigations, *Adv. Electron. Mater.*, 2024, 2400348.
43 A. F. I. Samer, H. Zyoud, A. F. I. Abdelkader and M. Shahwan, Numerical Modeling of High Conversion Efficiency Using SCAPS-1D Software, Mdpi, *Cystals*, 2021, **11**.
44 H. Movla, Optimization of the CIGS based thin film solar cells: Numerical simulation and analysis, *Optik*, 2014, **125**, 67–70.
45 J.-H. Yang, L. Shi, L.-W. Wang and S.-H. Wei, Non-Radiative Carrier Recombination Enhanced by Two-Level Process: A First-Principles Study, *Sci. Rep.*, 2016, **6**, 21712.
46 A. Kiligaridis, P. Frantsuzov, A. Yangui, S. Seth, J. Li, Q. An, Y. Vaynzof and I. G. Scheblykin, Are Shockley-Read-Hall and ABC models valid for lead halide perovskites? ABC model SRH+ model SRH model Excitation power density, *Nat. Commun.*, 2021, **12**, 3329.
47 S. R. Kavanagh, D. O. Scanlon, A. Walsh and C. Freysoldt, Impact of metastable defect structures on carrier recombination in solar cells, *Faraday Discuss.*, 2022, **239**, 339–356.
48 A. Alkauskas, C. Dreyer, J. L. Lyons and C. Van de Walle, Role of excited states in Shockley-Read-Hall recombination in wide-band-gap semiconductors, *Phys. Rev. B*, 2016, **93**, 201304(R).
49 M. Chen, M. Ju, H. F. Garces, A. D. Carl, L. K. Ono, Z. Hawash, Y. Zhang, T. Shen, Y. Qi, R. L. Grimm, D. Paci, X. C. Zeng, Y. Zhou and N. P. Padture, Highly stable and efficient all-inorganic lead-free perovskite solar cells with native-oxide passivation, *Nat. Commun.*, 2019, **10**, 16.
50 H. Menon and F. Yan, Device simulation and experimental validation of perovskite-cadmium telluride 4T tandem solar cell, *Front. Energy Res.*, 2024, **12**, 1–9.
51 M. Rahaman, M. Hasan, R. Moinuddin and M. N. Islam, Numerical optimization of lead-based and lead-free absorber materials for perovskite solar cell (PSC) architectures: A SCAPS-1D simulation, *AIP Adv.*, 2024, **14**, 095019.
52 M. S. Reza, A. Ghosh, N. Drissi, H. Al-Dmour, R. K. Prodhan, M. M. Islam, S. Begum, M. S. Reza and S. Sultana, Evaluation of design and device parameters for lead-free Sr3PBr3/Sr3NCl3 duel-layer perovskite photovoltaic device technology, *RSC Adv.*, 2024, **14**, 36675–36697.
53 K. Bhavsar and P. B. Lapsiwala, Numerical simulation of perovskite solar cell with different material as electron transport layer using SCAPS-1D software, *Semicond. Phys., Quantum Electron. Optoelectron.*, 2021, **24**, 341–347.
54 W. Zhang, C. You, Z. Dan, W. Wang and R. Dong, Improved performance of Cd-free CZTS thin-film solar cells by using CZTS0.4Se0.6BSF layer, *J. Phys.: Conf. Ser.*, 2023, **2418**, 0–7.
55 A. Ghosh, M. F. Islam Buian, M. Maniruzzaman, M. M. Hossain, A. K. Azad, A. A. Miazee, I. Ragab, A. A. Hassan, H. A. Alrafai and S. K. Alla Abdelrahim, Numerical analysis and device modelling of a lead-free Sr3PI3/Sr3SbI3 double absorber solar cell for enhanced efficiency, *RSC Adv.*, 2024, **14**, 26437–26456.
56 E. Danladi, P. M. Gyuk, N. N. Tasie, A. C. Egbugha, D. Behera, I. Hossain, I. M. Bagudo, M. L. Madugu and J. T. Ikyumbur, Impact of hole transport material on perovskite solar cells with different metal electrode: A SCAPS-1D simulation insight, *Heliyon*, 2023, **9**, e16838.
57 S. S. Hussain, Numerical Modeling and Optimization of Lead-Free Hybrid Double Perovskite, *J. Renewable Energy*, 2021, 668687.
58 E. Danladi, D. S. Dogo, S. U. Michael, F. O. Uloko and A. O. Salawu, Recent Advances in Modeling of Perovskite Solar Cells Using Scaps-1D: Effect of Absorber and Etm Thickness, *East Eur. J. Phys.*, 2021, **2021**, 5–17.
59 M. S. H. Rifat and M. Jahangir Alam, Exploring the Potential of Lead-Free Perovskite/Kesterite Double Absorber Structure With Diverse Transport Layer Materials to Enhance Tandem Solar Cell Performance, *IEEE Access*, 2024, **12**, 85115–85133.
60 J. L. Prasanna, E. Goel and A. Kumar, Defect Density-Dependent Dynamics of Double absorber layered Perovskite solar cell, *IEEE Photonics J.*, 2024, **16**, 1–10.
61 Z. Gao, X. He, W. Li and K. Xiong, Preprint not peer review Abstract: Preprint not peerved, 2015, vol. 2, p. 549.
62 S. Karthick, S. Velumani and J. Bouclé, Chalcogenide BaZrS3 perovskite solar cells: A numerical simulation and analysis using SCAPS-1D, *Opt. Mater.*, 2022, **126**, 112250.
63 J. M. Ball and A. Petrozza, Defects in perovskite-halides and their effects in solar cells, *Nat. Energy*, 2016, **1**, 16149.
64 A. Maiti, S. Chatterjee, L. Peedikakkandy and A. J. Pal, Defects and Their Passivation in Hybrid Halide Perovskites toward Solar Cell Applications, *Sol. RRL*, 2020, **4**, 1–31.
65 A. Mohandes, M. Moradi and H. Nadgaran, Numerical simulation of inorganic Cs2AgBiBr6 as a lead-free perovskite using device simulation SCAPS-1D, *Opt. Quantum Electron.*, 2021, **53**, 319.
66 C. Chen, Y. Yang, D. C. Bobela, S. Lu, K. Zeng, B. Yang, L. Gao, M. C. Beard and J. Tang, Characterization of basic physical properties of Sb_2Se_3, *Front. Optoelectron.*, 2017, **10**, 18–30.
67 M. Burgelman, Modeling thin-film PV devices, *Prog. Photovoltaics*, 2004, 143–153.
68 A. Ghosh, A. Al Hossain Newaz, A. Al Baki, N. S. Awwad, H. A. Ibrahium, M. S. Hossain, M. M. Rahman Sonic,

M. S. Islam and M. K. Rahman, Solar power conversion: CuI hole transport layer and Ba3NCl3 absorber enable advanced solar cell technology boosting efficiency over 30%, *RSC Adv.*, 2024, **14**, 24066–24081.
69 O. Access, halide perovskite absorber: SCAPS-1D and PVSyst analysis Accept United, 2024, pp. 1–11.
70 A. Zhang and R. Duan, Design and Numerical Investigation of CsPbI3/CsSn0.5Ge0.5I3 Double-Absorption-Layer Heterojunction Perovskite Solar Cells Based on SCAPS-1D, *Phys. Status Solidi A*, 2023, **220**, 1–13.
71 G. Haidari, Comparative 1D optoelectrical simulation of the perovskite solar cell, *AIP Adv.*, 2019, **9**, 085028.